

The cores of galaxies in the Coma cluster

Robert Minchin

April, 1997

Contents

1	Introduction	7
1.1	Historical Background	7
1.2	This project	10
2	Data Reduction	11
2.1	Image processing	11
2.1.1	The images	11
2.1.2	Cosmic ray removal	11
2.2	Ellipse fitting	12
2.2.1	Galphot - ellipfit	12
2.2.2	IRAF - ellipse	13
2.2.3	Checking the ellipse fits	13
2.2.4	Dusty galaxies	14
2.3	Data calibration	14
2.4	Other data	15
3	Analysis of data	16
3.1	Graphs from the ellipse fits	16
3.1.1	Isophote shapes	18

3.2	Images	18
3.3	Power laws	19
3.3.1	Fitting power laws	19
3.3.2	Information from the fit	19
3.3.3	Graphs from the power-law fits	21
3.3.4	Statistical analysis of power-law fits	21
4	Results	22
4.1	The Results	22
4.2	Differences between the two regions	22
4.3	M_v vs γ	27
4.3.1	Central region	27
4.3.2	Halo region	29
4.4	r_b vs γ	29
4.5	r_b & r_{lim} vs M_v	29
4.6	Break radius vs Effective radius	32
4.7	Comparison with previous results	34
4.7.1	M_v vs γ	34
4.7.2	r_b vs γ	34
4.8	Diskiness	34
4.9	Defining a Core	36
5	Conclusions	39
5.1	M_v vs γ	39
5.2	γ	39
5.3	M_v	39

5.4	r_b vs γ	40
5.5	r_b & r_{lim} vs M_v	40
5.6	Diskiness	40
5.7	Summary	40
A	Errors in the ellipses	42
B	Notes on Galaxies	44
C	Differentials of the Nuker Law	49
D	Computer programmes	51
D.1	Numerical Recipes routines	51
D.2	My routines	51
D.2.1	Project.c	51
D.2.2	Funcs.c	56

List of Tables

4.1	Semi-major axis fits	24
4.2	Average radius fits	25
4.3	Other galaxy data	26

List of Figures

1.1	Faber et al results for r_b vs M_v	9
3.1	Data from ellipse-fitting to NGC4889	17
3.2	Nuker-law fit to NGC4889	20
4.1	Data from the average-radius fit	23
4.2	Distribution of γ	28
4.3	Nuker-law fit to NGC4886	30
4.4	Plots of γ against M_v for the central and halo regions	31
4.5	r_b vs r_e and m_v	33
4.6	comparison to Faber et al's data	35
4.7	$\cos 4\theta$ terms for disk galaxies	37
4.8	Nuker-law fit to NGC4886	38

Abstract

I have analyzed HST images of 45 galaxies selected from the central and halo regions of the Coma cluster. A nuker-law fit to the profiles has been found and the relationships between the parameters of the nuker-law and between the total luminosity and isophote shape has been investigated. Problems were encountered with dust in the galaxies, with half of the galaxies in the sample suffering some degree of dust pollution. Where this was severe enough to affect the profile, the galaxy was excluded from the data set.

The differences between the central and halo regions have been investigated. It is predicted that core-type galaxies will form preferentially in the central region. This predicted relationship is not proven to exist although there is some evidence for it. Due to a difference in magnitudes between the two samples it is necessary for a relationship between γ and luminosity to exist in order to show preferential core formation in the central region. It is not possible to say that this relationship is definitely seen in the data.

Comparison of the data with previous results shows that the lack of cores seen in less-luminous galaxies could be an effect of resolution. This would create an artificial trend of γ with luminosity and an apparent dichotomy as only the steep outer power-law would be resolved in galaxies with smaller cores, giving a large value of γ . This trend and the values of γ higher than 0.3 could be a selection effect. Disky galaxies are seen to be able to form cores and a bright ($M_v < -22$) galaxy is seen with no resolved core.

Chapter 1

Introduction

1.1 Historical Background

Originally, cores were defined as the areas of constant surface brightness in the centre of the King (1966) model. This was shown by King (1978) to be a reasonable fit to the central regions of elliptical galaxies. Later CCD imaging showed that the King model did not describe adequately the surface brightness profiles of elliptical galaxies - the central regions were not, to the limit of resolution, areas of constant surface brightness. The regions now known as cores are regions of low logarithmic slope separated from the steeper outer logarithmic slope by a sharp break. The inner logarithmic slope does not go to zero as predicted by the King model (Lauer et al, 1995) at the limit of resolution.

Imaging of the cores of elliptical galaxies with the Hubble Space Telescope has allowed them to be examined at previously unattainable resolutions. The galaxies appear to divide into two types (Jaffe et al, 1994). Larger galaxies generally have profiles with well defined cores, described by a double power-law, whilst smaller galaxies can be described by a single power-law and have no well defined core (Bosch et al, 1994; Kormendy et al, 1994).

It is known that larger galaxies are triaxial systems supported by random motions and therefore having boxy isophotes while smaller galaxies are rotationally supported with disk isophotes (Davies et al, 1983). This division into two sorts of elliptical galaxies appears to correlate well with the division into those with and without unresolved cores (Kormendy et al, 1994; Jaffe et al, 1994).

Lauer et al (1995) fitted a 5-parameter double power-law to the inner profiles of galaxies. This law, known as the ‘Nuker’ law, fits both core-type and power-law galaxies well.

$$I(r) = I_b \times 2^{\frac{\beta-\gamma}{\alpha}} \times \left(\frac{r_b}{r}\right)^\gamma \times \left(1 + \left(\frac{r}{r_b}\right)^\alpha\right)^{\frac{\gamma-\beta}{\alpha}}$$

The parameters fitted by this law are the inner logarithmic slope, γ , the outer logarithmic slope, β , the sharpness of the break between the two slopes, α , the radius of the break, r_b and the intensity at the break, I_b . In terms of defining a core, γ is the most important as it shows the slope of the surface-brightness profile as it tends towards zero. It can be seen that for $r \ll r_b$, $I(r) \propto r^{-\gamma}$ and for $r \gg r_b$, $I(r) \propto r^{-\beta}$.

The results of fitting this law to a number of elliptical galaxies, and to the bulges of spiral galaxies, are given in Faber et al (1996). This classifies galaxies as having cores if $\gamma < 0.3$ and if the break is well-resolved. The claim is also made that there is a divide between the core-type galaxies and the power-law galaxies, which have $\gamma > 0.5$. The core-type galaxies are large, triaxial systems with $M_v < -20.5$ and the power-law galaxies are small, rotationally supported systems with $M_v > -22$.

Faber et al find that there is a clear division between the core and power-law profiles (see fig 1.1, from Faber et al 1996) which can be seen on the graph of r_b vs M_v and also as a gap in the distribution of γ between 0.3 and 0.5. Figure 1.1 also shows the division found into boxy and disk galaxies.

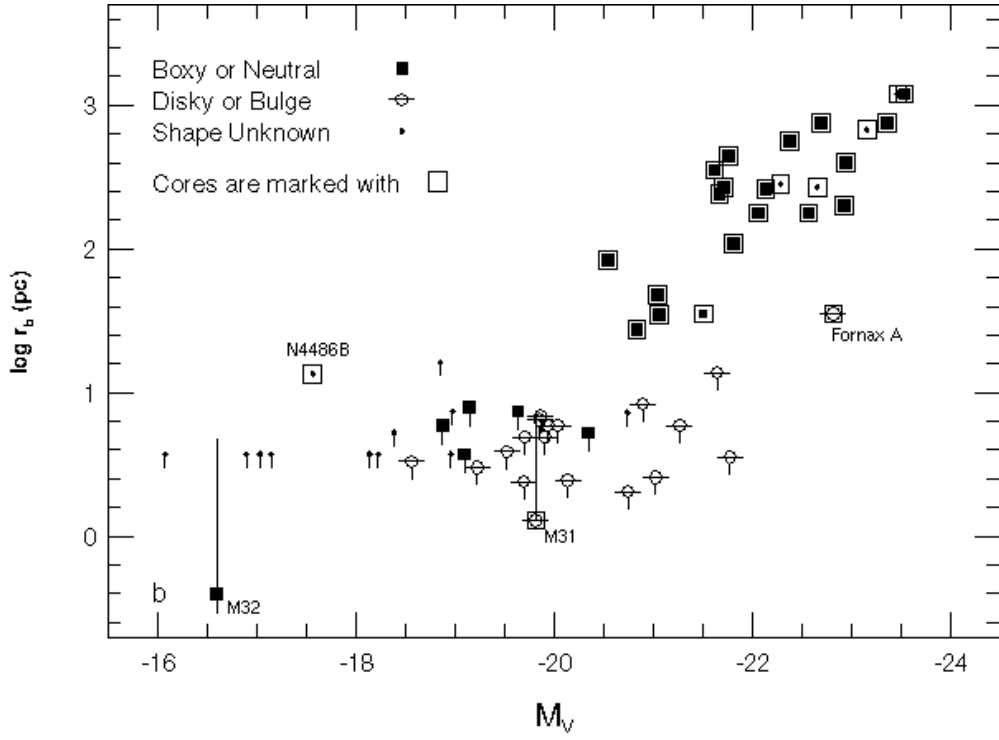


Figure 1.1: Faber et al results for r_b vs M_v

1.2 This project

Bender, Burstein and Faber (1992) proposed that the controlling factor in the evolution of a galaxy is the amount of gas present during formation and mergers. If there is a large amount of gas present then most of the energy is dissipated and the galaxy forms a small, rotationally supported (disky) system. Larger galaxies are formed later by mergers of these smaller galaxies when most of the gas has formed into stars. These stellar mergers do not dissipate energy and so form triaxial systems. This theorem is called the gas/stellar continuum (GS continuum). Faber et al (1996) puts forward this theorem as explaining why disk galaxies show power-laws as the gas in dissipative mergers is carried towards the centre of the galaxies.

The Coma cluster provides a good test area for this theory as the central region consists of a dynamically relaxed system where the galaxies have interacted frequently and have little gas and the halo region consists of relatively gas-rich galaxies which have not yet visited the core and have had little chance to interact. The cluster is rich enough to be able to form a statistically significant sample of both regions and projection of HST data from the Virgo cluster has shown that it is possible to distinguish the two kinds of profiles at the distance of the Coma cluster.

If the GS continuum theorem is correct, it should be possible to see preferential formation of power-law galaxies in the halo region and preferential formation of core-type galaxies in the central region. This should result in there being a significant difference between the distributions of γ for the two samples. I will also examine the relationships seen by Faber et al in their survey to determine if these are seen in the Coma cluster.

There are 45 galaxies in the sample, 23 from the central region of Coma and 22 from the halo. In chapters 2 and 3 I explain how the images were reduced and the data analysed. In chapter 4 I present my results and in chapter 5 I give my conclusions. The derivation of the error in the surface-brightness profile and notes on the galaxies are given in an appendix.

Chapter 2

Data Reduction

2.1 Image processing

2.1.1 The images

The Hubble Space Telescope was used to obtain 2 WFPC/2 images of each of the 45 galaxies in the sample. The Planetary Camera images were extracted and trimmed from [1:800,1:800] to [55:798,55:798] in order to remove noise around the bottom and left edges of the plates. The images were examined and those with suspected dust noted.

2.1.2 Cosmic ray removal

Cosmic ray interference was reduced by combining the two images of each galaxy using the IRAF routine imcombine with the parameters reject=crreject, hsig=2.5, gain=7. These parameters tell the routine to look for objects that resemble cosmic rays - sharply defined bright (positive) points - and remove them if they are more than 2.5 times the expected variation from the value on the other image. The gain value of 7 was obtained from the image headers and defines how many photon counts there are for each ADU.

In order to ensure the alignment of the two images prior to combining them, the IRAF routine `center` was used to find the centre of each image. From this the offset between the centres in the pair was found and those galaxies with an offset of less than 0.2 pixels were combined, those with an offset of greater than 0.1 pixels being noted (see Appendix B).

Four galaxies had offsets outside of this range, these were examined using the IRAF routine `X-register`. This routine performs a cross-correlation over a wide area rather than finding the centre. This routine gave two of the galaxies as having shifts less than 0.1 pixels, these were combined. The remaining two galaxies were shifted using `X-shift` prior to being combined (see Appendix B).

2.2 Ellipse fitting

A working notation of naming the galaxies c01 to c45 was introduced with c01 to c23 being in the core (angular distance from the cluster centre less than $0.7^\circ \approx 1$ Mpc), as defined in Lucey et al (1991), and c24 to c45 being in the halo. This notation allowed automated routines to be run easily and the core and halo galaxies to be easily distinguished. Header files were constructed for each galaxy containing the proper names, exposure times and other data from literature.

2.2.1 Galphot - ellipfit

The Galphot routines by R Peletier were used to fit ellipses to the galaxies. The routines identified stars and remaining cosmic rays and masked them out. Problems with this masking, such as unmasked diffraction spikes, were corrected manually and a manual masking routine was also used to remove dust lanes. A map of bad pixels was also constructed and added to the mask.

An initial fit was made using the `harmfit` routine. This fits circular isophotes with harmonics. This produced a residual image which could be used to check the mask.

The final fit was made using the `ellipfit` routine. This fits elliptical isophotes for a number of iterations then fits harmonic terms to these isophotes. The routine creates a residual image after

each iteration and uses this to correct itself thus giving it good accuracy. The fit is done using annuli of 5% of the radius at 10% intervals. Outside 20 pixel radius the fit is done to all the pixels that are inside the annulus, within this radius the width of the annulus is less than 1 pixel so interpolation is used to calculate the values.

2.2.2 IRAF - ellipse

The IRAF routine ellipse was used as a check to the Galphot fits. This routine fits by sampling a number of sectors around annuli and using these to construct ellipses. The routine appears less reliable than the Galphot routines, as it uses a cruder fitting method, but produced comparable output.

In order to run this routine, two IRAF scripts were used. The first ran an initial fit over 2 to 60 pixels radius and was seeded using 4 points - the ends of the major and minor axes - found from an isophote contour map of the galaxy. The second script used the largest reliable fit (indicated by the programme returning a stop-value of 0, meaning that the fit had been trouble free) from the first fit and ran over the range 2 to 400 pixels radius. For this second fit a minimum value for the intensity slope was specified in order to stop the ellipses overlapping at low intensities. At these low intensities (high radii) fitting was done concentrically with the ellipticity and centre-position held constant.

2.2.3 Checking the ellipse fits

The ellipses used were those produced by the Galphot routines. The fits produced were consistent with those from the IRAF routine. The residuals produced by Galphot were also checked, this often showed dust that had been missed on a prior inspection of the image as the dust led to large residuals being formed.

2.2.4 Dusty galaxies

A number of galaxies are badly affected by dust. If there were serious features caused by dust after masking of visible dustlanes, an entry was made into the header files of these galaxies and they were not included in the sample. This excluded 6 galaxies from the central region and 5 from the halo region.

About half of the sample were affected by dust but half of these were not seriously affected - the dust lanes were thin enough to be masked out without any major loss of information.

2.3 Data calibration

The data tables were read into Super Mongo. The data was calibrated from ADU to magnitudes using the equation

$$m = -2.5 \times \log \left(\frac{PHOTFLAM \times DN}{EXPTIME} \right) + PHOTZPT$$

from the WFPC/2 instrument handbook, where DN is the number of counts, PHOTFLAM and PHOTZPT are photometric calibration constants (the sensitivity and zero point of the CCD's) which have the values 1.88 and -21.1 respectively for this data and EXPTIME is the exposure time. The values for these were obtained from the image header files. EXPTIME was not constant over the set of readings, being 400 seconds for the fainter galaxies, 200 seconds for the majority of galaxies in the sample and 160 seconds for the dominant galaxy, NGC4889. The distance scale was calibrated using 1 pixel = 0.046 arcseconds. This allowed the surface brightness to be found in terms of magnitude arcsec⁻².

2.4 Other data

The magnitude of the galaxies in the v-band was found from measurements of A_e and Sb_e carried by Lucey et al (1991). The distance to Coma was taken from Faber et al (1996) as 7461 km s^{-1} . A value of $H_0 = 80 \text{ km s}^{-1} \text{ Mpc}^{-1}$ was used to calculate the absolute magnitudes and the angular scale as this was the value adopted by Faber et al.

The header files eventually contained the proper names, exposure times, distances from the centre of the Coma cluster (in degrees), effective diameter and average surface brightness within this diameter and whether the galaxy was seriously affected by dust. The data on the distances from the centre of Coma, the effective diameter and the effective surface brightness were those from Lucey et al mentioned above. I made the judgement on whether the galaxies were badly affected by dust - if there were problems due to dust which prevented ellipses being fitted over an extended region or if the profile was distorted by dust so it could not be well fitted by a power-law then the galaxy was defined as being badly affected by dust.

Chapter 3

Analysis of data

3.1 Graphs from the ellipse fits

Graphs were made using Super Mongo by reading in the data files produced by the ellipfit routine in galphot. The data were calibrated so that ADU were converted to magnitudes and distances were in arcseconds. Data from the IRAF ellipse routine were also read in and graphed. This provided a check on the galphot data.

The surface brightness per arcsecond squared, position angle, ellipticity, deviation of the centre in x and y, and the harmonics for 3θ and 4θ were plotted against the log of a, the semi-major axis. For data from galphot, a was calculated using $a = \frac{r}{\sqrt{1-\epsilon}}$ where ϵ is the ellipticity. This conversion was unnecessary for ellipse data as it used a rather than r for its scaling.

The ellipse data matched well with the galphot data in most of the graphs. The galphot data alone was used for analysis.

An example of the graphs obtained is given in figure 3.1, this is of the D-type galaxy NGC4889 (c13 in my numbering scheme). The results from Galphot are shown by crosses and the results from IRAF are shown by boxes.

NGC4889
C13

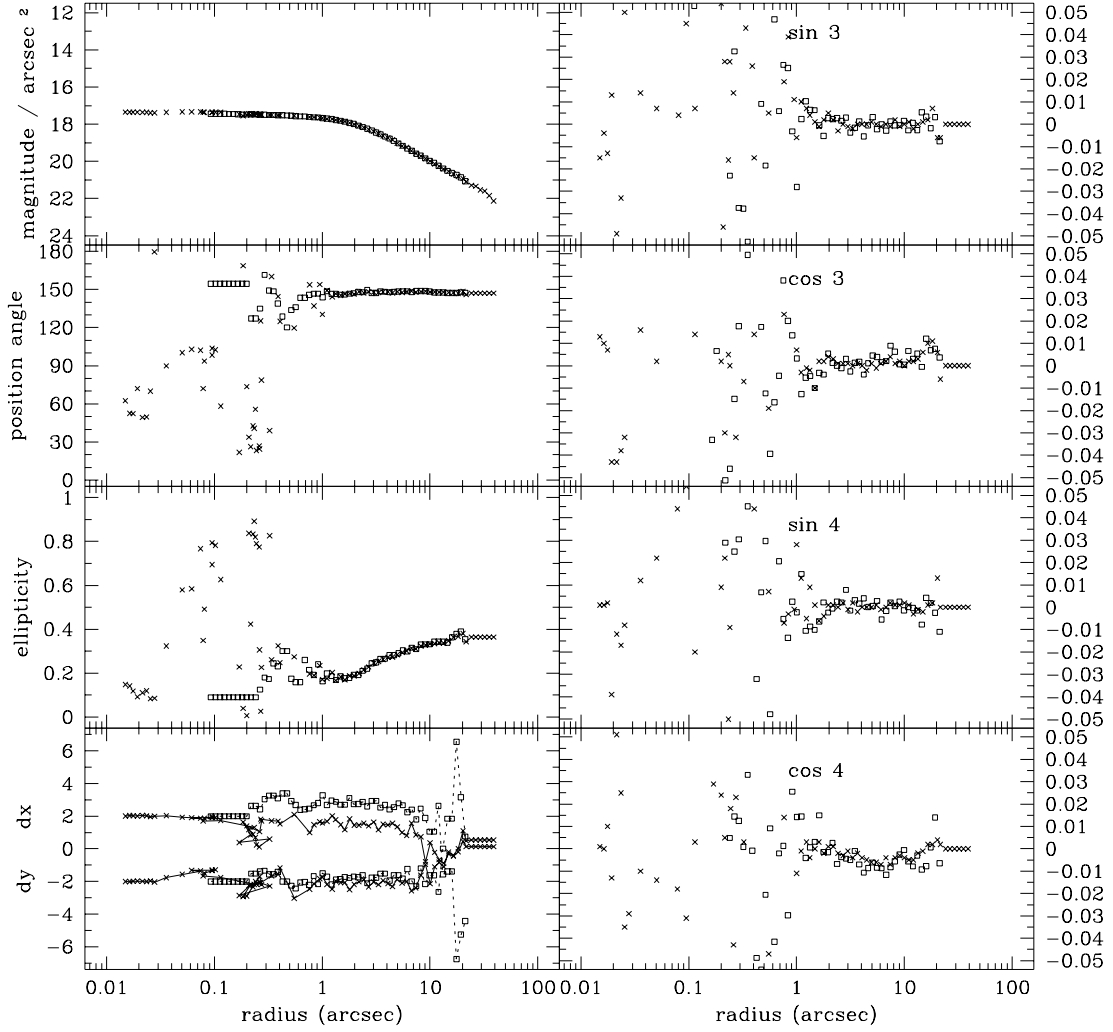


Figure 3.1: Data from ellipse-fitting to NGC4889

3.1.1 Isophote shapes

The range over which the profile appeared reliable was from a radius of 2 pixels to a surface brightness of $20.5 \text{ mag arcsec}^{-2}$. The highest absolute value reached by the $\cos 4\theta$ term in this region was used to determine whether the galaxy appeared to be boxy or disky.

A Super Mongo routine was written to return the highest absolute value. This value was then converted to a_4/a by dividing by 1.4 (conversion factor from Pelatier, 1989). This figure shows the distortion of the ellipse into a boxy or disky shape, disky shapes having positive values. For the purposes of definition, galaxies with $a_4/a > 0.02$ were said to be disky, if this value was not being returned due to distortions due to dust.

3.2 Images

Black and white greyscale images were obtained using the print function within SAOimage. They showed the outer part of the galaxies, scaled logarithmically from 0% to 10% of the luminosity, the core of the galaxies, scaled logarithmically from 4% to 100% of the luminosity, and the residuals left by galphot. The outer parts and the residuals were at $\times 1$ magnification and the cores were at $\times 4$ magnification with the exception of NGC4889, the cD galaxy, which was shown at $\times 2$ magnification.

The greyscales were examined for signs of visible dust and galaxies thus identified were added to the list of galaxies already noted as containing dust. The residuals were also examined and those with large residuals in the centre were re-fitted. Most of the large residuals were due to severe dust contamination and only small improvements in the fit were possible.

3.3 Power laws

3.3.1 Fitting power laws

A computer programme was written to fit the nuker law to the surface brightness profile using a simulated annealing (Levenberg-Marquadt) routine from Numerical Recipes (Press et al, 1992) to find the five parameters. The fit was made to both semi-major axis and average-radius profiles between 2 pixels and $20.5 \text{ mag arcsec}^{-1}$, the limits that appear to be the limit of resolution and the point where sky effects become important.

A proportional error in the number of counts (DN) of $P_{\langle DN \rangle} = \frac{\sqrt{g \times \langle DN \rangle + \sigma_{rn}^2}}{g \times \langle DN \rangle \times \sqrt{2\pi r \delta r}}$ was used in the input data (see Appendix) where $\langle DN \rangle$ is the average number of counts (in ADU) in an annulus, r is the inner radius of the annulus, δr is the width of the annulus, g is the gain and σ_{rn} is the read noise.

The read noise is taken to be $\frac{5}{\sqrt{2}}$ as each image has a read noise of 5 and two images were averaged. The gain is taken to be 14 as each image has a gain of 7 so 14 photons are needed for each ADU.

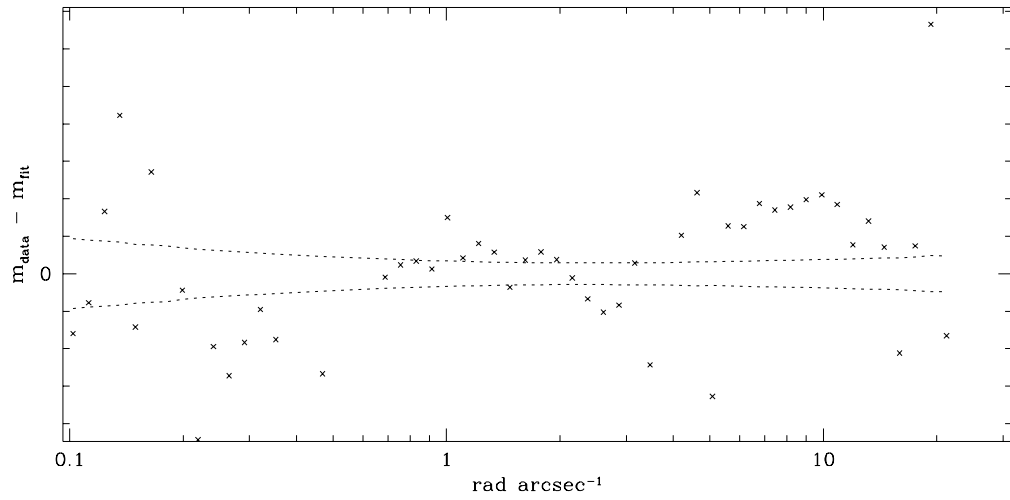
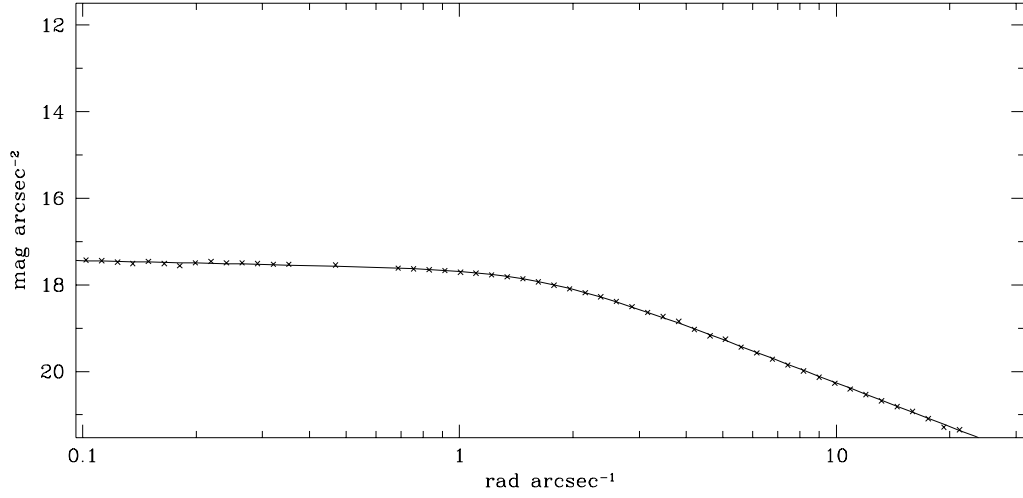
3.3.2 Information from the fit

The fit returned values and errors for the 5 parameters needed for the nuker law (α , β , γ , r_b , I_r). These were used to construct a model profile which was compared with the original to check whether the fit was satisfactory. If the errors associated with the constants of the fit were too large or the fit did not match the original data the fit was rejected as unsatisfactory.

An example graph is given in fig. 3.2 of NGC4889, showing the datapoints with the fit through them in the top half and the difference between the fit and the datapoints, with the line of error around the datapoints, in the bottom half.

The fit was unable to fit satisfactorily to some of the profiles, these were removed from the

NGC4889
C13



$\alpha = 3.265952$ $\beta = 1.341839$ $\gamma = 0.071643$ $r_b = 1.677052$ $I_b = 0.065948 \times 10^{-6}$ $X = 2949.185059$
 $\delta\alpha = 0.022504$ $\delta\beta = 0.000902$ $\delta\gamma = 0.001300$ $\delta r_b = 0.002877$ $\delta I_b = 0.000089 \times 10^{-6}$ $X_v = 61.441357$
 initial values: $\alpha = 2.000000$ $\beta = 1.000000$ $\gamma = 0.050000$ $r_b = 1.000000$ $I_b = 0.100000 \times 10^{-6}$

Figure 3.2: Nuker-law fit to NGC4889

sample. This removed 4 galaxies, all of them from the central region, on the semi-major axis fits and 7 galaxies, all but one from the central region, on the average-radius fits. Another galaxy was removed from the central region in the average-radius fits as it had an inner logarithmic slope, γ , that indicated a core but its break radius was too close to the limit of resolution to be considered reliable, as was one from the outer regions on the semi-major axis fit.

For the average-radius fit, this left 10 galaxies in the central region and 16 in the halo. For the semi-major axis fits, this left 13 galaxies in the central region and 16 in the halo.

The parameters returned for each galaxy are given in tables C-1 (semi-major axis fits) and C-2 (average-radius fits) and the graphs obtained from these are also given.

3.3.3 Graphs from the power-law fits

The values of γ and r_b from the nuker-law fits and the values of m_v and distance from the centre of Coma were plotted against each other in 6 graphs of apparent values and 6 graphs of absolute values. Only those galaxies left in the sample, as detailed above, were graphed. These graphs were examined for trends and for differences between the samples from the inner and outer regions of Coma.

3.3.4 Statistical analysis of power-law fits

The Kolomogrov-Smirnov two-sample test was used to examine differences between the samples. This test gives the confidence that two samples are from the same parent population. Details of the test were found in Wall (1977). This test was used to look for differences in magnitude and γ .

Chapter 4

Results

4.1 The Results

The results are given of fits to both the semi-major axis and the average-radius in tables 4.1 and 4.2. Additional information is given in table 4.3. Data from the average-radius fit is shown graphically in figure 4.1 with crosses representing galaxies from the central region and boxes representing galaxies from the halo region.

4.2 Differences between the two regions

The Kolomogrov-Smirnov test showed that the distributions of γ in the two regions were likely to be from the same parent distribution, eg. there was no significant difference between them. Using the same test, the probability that the magnitudes were from the same parent distribution was tested and was found to be in the 5% tail of the normal distribution, eg. the distributions of the magnitudes were fairly significantly different.

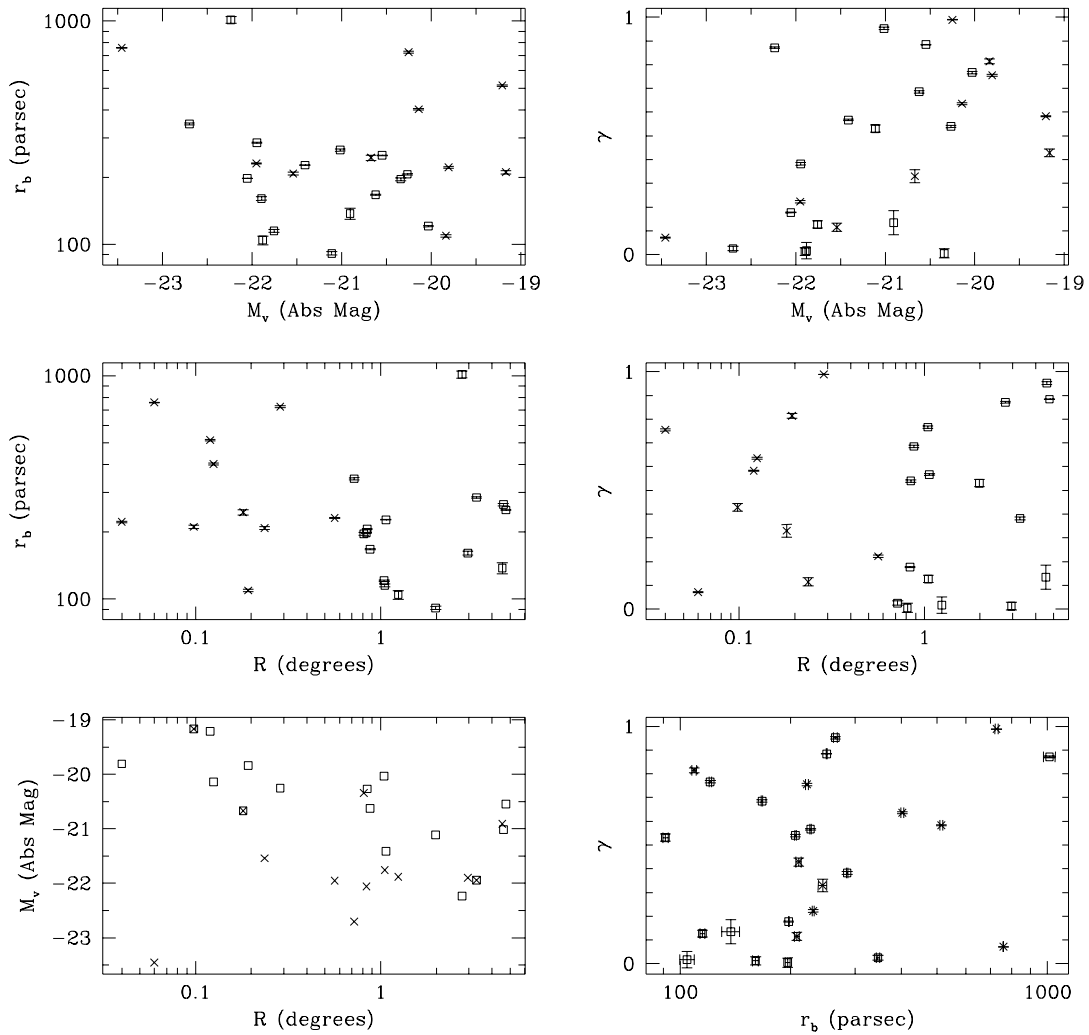


Figure 4.1: Data from the average-radius fit: crosses = central, boxes = halo except for m_v vs R

- crosses = $\gamma < 0.3$, open boxes = $\gamma > 0.5$, boxed cross = $0.3 < \gamma < 0.5$

name	α	β	γ	r_b^a	θ_b^b	μ_b^c	Status ^d
NGC4886	17.31	1.257	0.8129	139	0.3071	17	0
IC4011	0.0549	1.255	1.219	354.6	0.7834	18.82	2
NGC4876	0.6783	1.852	0.005982	245.5	0.5423	17.72	1
RB43	3	1.5	1.513	427.5	0.9444	18.95	2
IC3959	1.963	1.681	0.06006	304.9	0.6736	17.71	1
IC3957	3	1.461	0.03316	41.19	0.091	15.38	1
RB257	2	7.549	1.102	3157	6.976	23.37	1
RB260	0.4373	2.09	0.03839	225.9	0.4992	18.65	0
NGC4869	1.124	1.687	0.04334	310.6	0.6863	17.69	1
RB6	2.423	1.615	0.5326	913.7	2.019	19.78	0
RB45	3.23	1.413	0.7533	222.2	0.4909	18.09	0
RB18	1.971	1.416	0.4456	277.7	0.6136	18.82	0
NGC4889	2.598	1.318	0.05961	876.8	1.937	17.98	0
IC4021	2	1.711	1.043	483.9	1.069	18.75	2
RB167	1.612	1.455	0.01836	184	0.4066	17.65	1
IC4012	1.523	1.867	0.6039	441.1	0.9746	18.25	0
IC3947	3.181	1.789	0.9645	1226	2.709	19.74	0
RB234	7.854	1.33	0.8507	115.9	0.2561	17.66	0
IC4051	0.563	1.646	0.01028	386.6	0.8542	18.36	0
NGC4860	0.6315	2.473	0.02111	778.6	1.72	18.53	0
RB241	2	1.352	0.9355	223.4	0.4937	17.48	2
NGC4906	0.9332	1.748	0.3634	399	0.8815	18.3	0
NGC4926	1.635	1.566	0.2113	272	0.6009	16.96	0
NGC4816	4.698	1.345	0.1717	215.2	0.4755	16.98	0
Zw160-23	1.292	1.712	0.0567	238.8	0.5276	17.59	0
IC3618	4.343	1.678	0.8824	279.3	0.6172	17.51	0
Zw159-43	0.954	1.694	0.2694	176.5	0.3899	16.71	0
IC3623	2.488	1.433	0.9394	200.9	0.444	17.08	0
NGC4673	0.8752	1.927	0.2442	357.2	0.7892	16.83	0
NGC4692	1.305	1.328	0.8405	717.4	1.585	18.35	0
Zw159-83	3	1.658	0.8535	1130	2.497	19.14	1
Zw159-89	1.123	1.346	0.01302	56.33	0.1244	16.14	3
IC832	0.2229	2.223	0.01205	406.2	0.8974	18.3	1
NGC4789	1.59	1.337	0.003033	180.3	0.3983	16.52	1
NGC4807	2.802	1.521	0.5721	239.6	0.5293	16.78	0
IC834	2	1.638	0.01575	184.6	0.408	16.55	1
NGC4824	2.751	1.629	0.5161	224.9	0.4969	17.6	0
NGC4827	2.464	1.37	0.4234	180.2	0.3981	16.56	0
NGC4839	1.121	1.322	0.05773	346.2	0.7649	17.79	0
NM8603	4.491	1.341	0.6988	130	0.2872	17.15	0
IC4133	3.373	1.601	0.7037	185.3	0.4094	17.03	0
NGC4952	1.043	1.47	0.243	147.6	0.3261	16.1	1
NGC5004	1.24	1.449	0.02914	176.6	0.3902	16.61	0
NGC4957	0.975	1.362	0.002576	122.7	0.2711	16.65	0
Zw160-159	1.836	1.428	1.085	421.8	0.932	18.17	0

^aBreak radius in parsec

^bBreak radius in arcsec

^csurface brightness in mag arcsec⁻² at the break radius

^d0 = Okay, 1 = Dusty, 2 = Unsatisfactory fit, 3 = Break radius less than limit of resolution (1.6 arcsec)

Table 4.1: Semi-major axis fits

name	α	β	γ	r_b^a	θ_b^b	μ_b^c	Status ^d
NGC4886	2	1.284	0.4267	82.36	0.182	16.53	2
IC4011	1	1.272	0.00273	2.855	0.006307	13.15	2
NGC4876	0.6578	1.892	0.0076	234.8	0.5187	17.79	1
RB43	3.567	1.486	1.539	674.7	1.491	19.82	2
IC3959	2.022	1.623	0.03834	257.7	0.5694	17.65	1
IC3957	2	1.477	0.02171	30.68	0.06779	15.13	1
RB257	2	2.684	1.12	974.9	2.154	20.3	1
RB260	1.509	1.312	0.01441	56.32	0.1244	17.39	3
NGC4869	1.14	1.642	0.06591	261	0.5767	17.63	1
RB6	3.35	1.426	0.5831	514.7	1.137	19.53	0
RB45	3.129	1.411	0.7549	221.5	0.4893	18.1	0
RB18	1.904	1.426	0.4283	210.5	0.465	18.7	0
NGC4889	3.266	1.342	0.07164	759	1.677	17.95	0
IC4021	2	1.711	1.043	459.1	1.014	18.75	2
RB167	1.619	1.455	0.01015	143.5	0.317	17.66	1
IC4012	1.884	1.886	0.6361	403.1	0.8906	18.27	0
IC3947	5.202	1.675	0.9887	727	1.606	19.28	0
RB234	5.209	1.338	0.8142	109.3	0.2415	17.64	0
IC4051	0.4025	2.538	0.000369	2438	5.388	20.51	2
NGC4860	1.124	1.657	0.115	207.9	0.4593	17.13	0
RB241	0.1946	2.523	0.03161	478.1	1.056	18.57	2
NGC4906	0.9681	1.592	0.3301	244.4	0.54	17.88	0
NGC4926	1.746	1.512	0.2227	230.5	0.5094	16.92	0
NGC4816	4.879	1.359	0.1777	197.7	0.4368	16.98	0
Zw160-23	1.093	1.726	0.005016	196.2	0.4336	17.53	0
IC3618	6.347	1.699	0.8842	250.5	0.5534	17.39	0
Zw159-43	0.8081	1.83	0.1348	137.4	0.3037	16.58	0
IC3623	1.78	1.498	0.9522	264.9	0.5852	17.59	0
NGC4673	1.279	1.744	0.3826	285.1	0.6298	16.66	0
NGC4692	1.139	1.419	0.8713	1013	2.239	18.89	0
Zw159-83	2	1.878	0.8326	1294	2.86	19.5	1
Zw159-89	3.552	1.224	0.5308	91.26	0.2016	16.55	0
IC832	2	1.625	0.971	1174	2.593	19.67	1
NGC4789	1.588	1.337	0.006029	160.8	0.3553	16.52	1
NGC4807	2.554	1.555	0.5669	226.7	0.5008	16.83	0
IC834	2	1.639	0.001654	155.3	0.343	16.55	1
NGC4824	2.822	1.595	0.54	206.2	0.4556	17.59	0
NGC4827	1.74	1.398	0.1269	115.1	0.2543	16.25	0
NGC4839	1.156	1.368	0.02589	345.8	0.7641	17.89	0
NM8603	5.912	1.361	0.7665	120.9	0.2671	17.16	0
IC4133	2.964	1.578	0.6853	167.1	0.3693	16.96	0
NGC4952	1.029	1.471	0.2141	118.6	0.262	16.06	1
NGC5004	1.16	1.51	0.01231	160.6	0.3549	16.62	0
NGC4957	1.093	1.355	0.01682	104.5	0.2309	16.58	0
Zw160-159	0.1112	2.621	0.04299	567	1.253	18.74	2

^aBreak radius in parsec

^bBreak radius in arcsec

^csurface brightness in mag arcsec⁻² at the break radius

^d0 = Okay, 1 = Dusty, 2 = Unsatisfactory fit, 3 = Break radius less than limit of resolution (1.6 arcsec)

Table 4.2: Average radius fits

name	mag ^a	radius ^b	abs mag ^c	c4 ^d	a4 ^d
NGC4886	13.93	0.05	-20.92	0.01	0.007143
IC4011	14.87	0.064	-19.98	0.009	0.006429
NGC4876	14.34	0.062	-20.51	-0.62	-0.4429
RB43	15.37	0.056	-19.48	-0.012	-0.008571
IC3959	13.99	0.245	-20.86	0.532	0.38
IC3957	15.2	0.259	-19.65	0.027	0.01929
RB257	15.44	0.209	-19.41	0.014	0.01
RB260	15.75	0.192	-19.1	0.013	0.009286
NGC4869	13.52	0.119	-21.33	0.031	0.02214
RB6	15.64	0.12	-19.21	0.029	0.02071
RB45	15.04	0.04	-19.81	0.015	0.01071
RB18	15.68	0.098	-19.17	0.04	0.02857
NGC4889	11.39	0.06	-23.46	-4.273	-3.052
IC4021	14.78	0.112	-20.07	0.015	0.01071
RB167	14.78	0.212	-20.07	-0.184	-0.1314
IC4012	14.71	0.125	-20.14	-0.091	-0.065
IC3947	14.6	0.287	-20.25	0.032	0.02286
RB234	15.01	0.193	-19.84	0.012	0.008571
IC4051	13.02	0.234	-21.83	0.028	0.02
NGC4860	13.31	0.236	-21.54	0.043	0.03071
RB241	13.81	0.304	-21.04	0.006	0.004286
NGC4906	14.18	0.181	-20.67	0.019	0.01357
NGC4926	12.9	0.565	-21.95	0.018	0.01286
NGC4816	12.79	0.839	-22.06	-0.042	-0.03
Zw160-23	14.51	0.811	-20.34	0.027	0.01929
IC3618	14.3	4.75	-20.55	0.037	0.02643
Zw159-43	13.94	4.545	-20.91	0.011	0.007857
IC3623	13.83	4.604	-21.02	0.015	0.01071
NGC4673	12.9	3.294	-21.95	-0.013	-0.009286
NGC4692	12.61	2.75	-22.24	-0.02	-0.01429
Zw159-83	13.45	2.5	-21.4	-0.082	-0.05857
Zw159-89	13.74	1.986	-21.11	0.039	0.02786
IC832	13.69	2.01	-21.16	-0.063	-0.045
NGC4789	12.39	1.525	-22.46	0.006	0.004286
NGC4807	13.44	1.067	-21.41	-0.014	-0.01
IC834	13.79	1.794	-21.06	0.02	0.01429
NGC4824	14.58	0.846	-20.27	0.014	0.01
NGC4827	13.09	1.053	-21.76	-13.71	-9.793
NGC4839	12.15	0.719	-22.7	0.498	0.3557
NM8603	14.82	1.046	-20.03	0.021	0.015
IC4133	14.23	0.879	-20.62	0.015	0.01071
NGC4952	12.82	1.609	-22.03	0.036	0.02571
NGC5004	12.95	2.959	-21.9	0.042	0.03
NGC4957	12.97	1.246	-21.88	-0.013	-0.009286
Zw160-159	13.92	2.79	-20.93	0.013	0.009286

^aCalculated from V-band measurements of A_e and SB_e

^bDistance from centre of Coma cluster in degrees

^cCalculated from apparent magnitude taking $H_0 = 80 \text{ Mpc}^{-1} \text{ km s}^{-1}$

^d $\cos 4 \theta$ deviations from ellipse and $a4/a$ deviation from ellipse, calculated from $c4$ by dividing by 1.4

Table 4.3: Other galaxy data

The galaxies in the halo region were on the whole a magnitude brighter than the galaxies in the central region, both regions had the same distribution of γ in their samples. If there is a trend of γ with M_v , this would show that there was a difference in the formation of core-type galaxies between the halo and central regions.

4.3 M_v vs γ

Examination of the graph of M_v against γ does not show any definite trend. 3 out of 4 galaxies brighter than -22 magnitudes show cores, indicating that larger galaxies generally contain cores. There do not appear to be many smaller galaxies with cores but it is impossible to say whether this reflects a physical effect or whether this is an artefact of resolution.

There are 3 points in the region $0.3 < \gamma < 0.5$, For a uniform distribution between 0 and 1, which encompasses all the values in the data set, 5.4 points would be expected in this region. The expected counting error on this is therefore $\sigma = \sqrt{5.4} = 2.3$, this means that the number of points found in this region is barely significantly less than would be expected from a uniform distribution. It is still the case that this region has a lower number density than the core or power-law regions either side of.

The frequency distribution of the γ 's of galaxies (from the average-radius fit) is shown in fig 4.2. The shaded area represents galaxies in the halo region, the clear area represents galaxies in the central region.

4.3.1 Central region

There is only one bright galaxy in the sample, NGC4889. This is one of two D-galaxies in the central region of Coma and shows a definite core. Due to cannibalisation by the two D-galaxies, there are no other bright galaxies in this region, this is a contributing factor to the difference in magnitudes between the two regions.

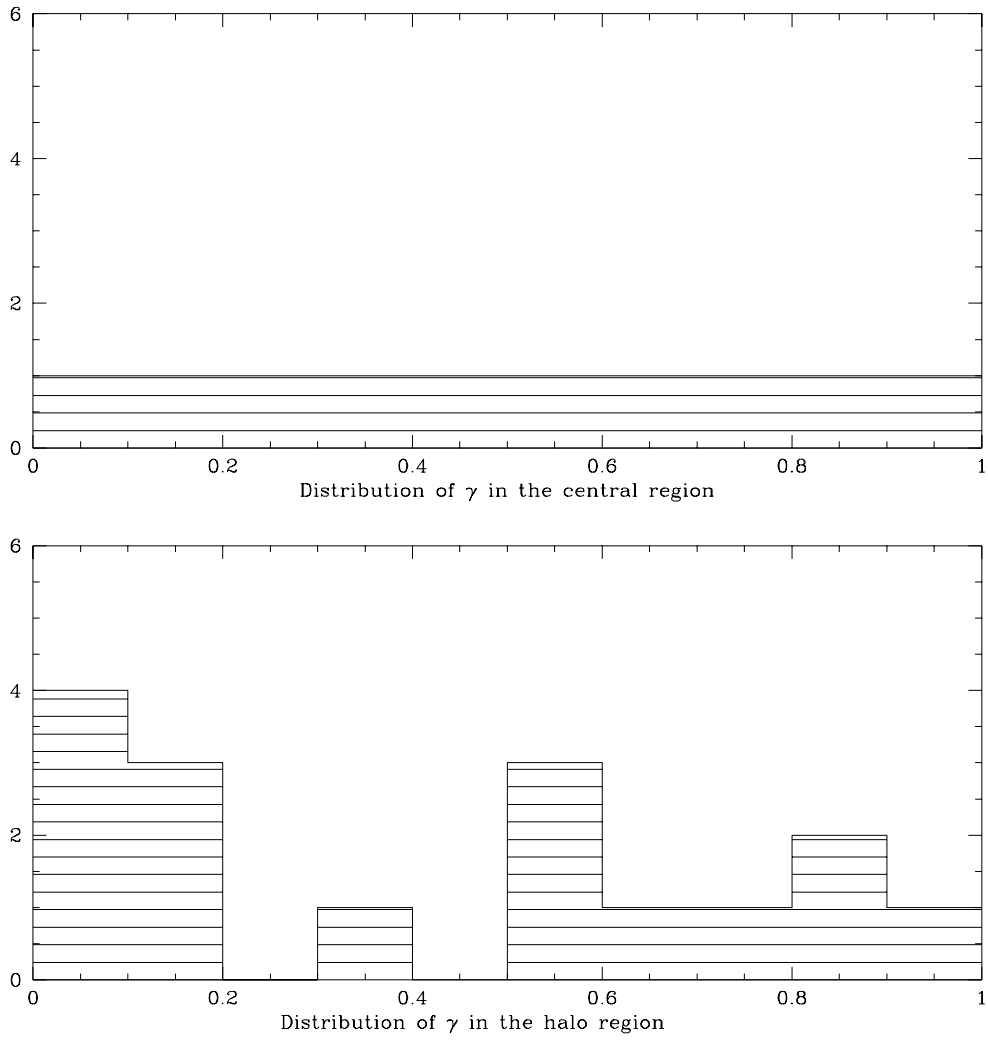


Figure 4.2: Binned distribution of γ for the central region (upper graph) and the halo region (lower graph)

The evidence for a trend in γ with M_v is fairly good in this region (see fig 4.4), although this could be a selection effect due to the smaller low-luminosity galaxies. two of the galaxies in the intermediate zone $0.3 < \gamma < 0.5$ are in the central region, exactly the number that would be expected for a uniform distribution between 0 and 1 and the same number density as is seen in all bins when γ is binned in tenths (see fit 4.2).

4.3.2 Halo region

There are 3 bright galaxies in the sample (defined as being in the $M_v < -22$ region where Faber et al find no cores), two of them show definite cores but the third (NGC4692) has a single power-law through to the limit of resolution (see fig 4.3). There are few faint galaxies in the sample due to the lack of comprehensive surveying in the halo region of Coma.

There is only 1 galaxy in the intermediate zone in the halo region, even if this region is extended to cover $0.2 < \gamma < 0.5$. There does appear to be a well-defined gap (see fig 4.2) This region shows virtually no correlation of γ with M_v (see fig 4.4)

4.4 r_b vs γ

Taking the values returned by the fit, there is a fairly even distribution of break radii (see fig 4.1). If it is assumed that the cores are unresolved for $\gamma > 0.5$ then all these galaxies have break radii smaller than the limit of resolution, $r_{lim} = 70$ pc (limit of resolution given by $\log r_b$ (arcsec) = -0.8, as used in Faber et al).

4.5 r_b & r_{lim} vs M_v

Faber et al claim values for r_{lim} much smaller than their value used for the limit of resolution for the cores by examining deconvolved profiles within 0.1 arcsec and comparing these with a

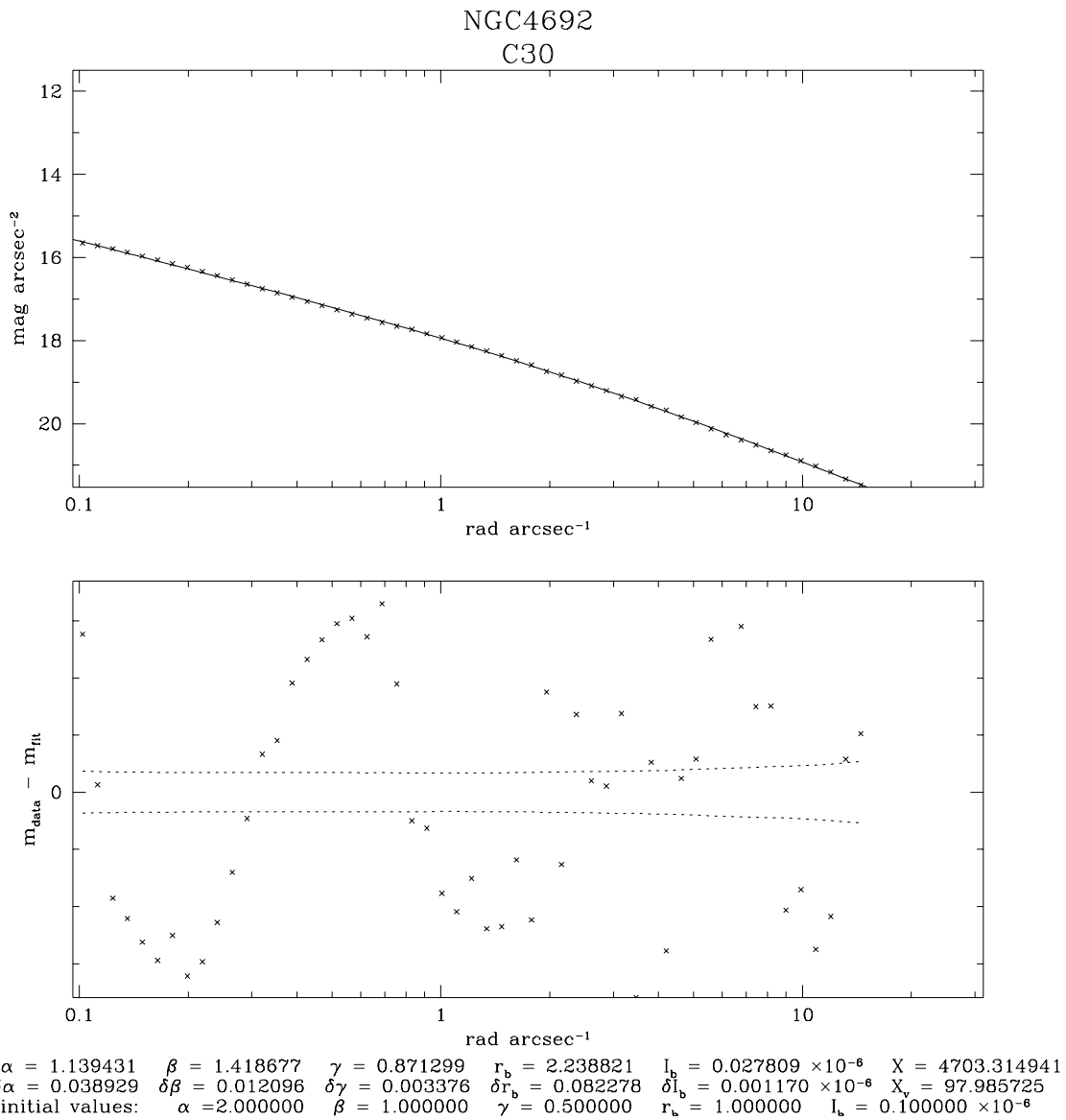


Figure 4.3: Nuker-law fit to NGC4886

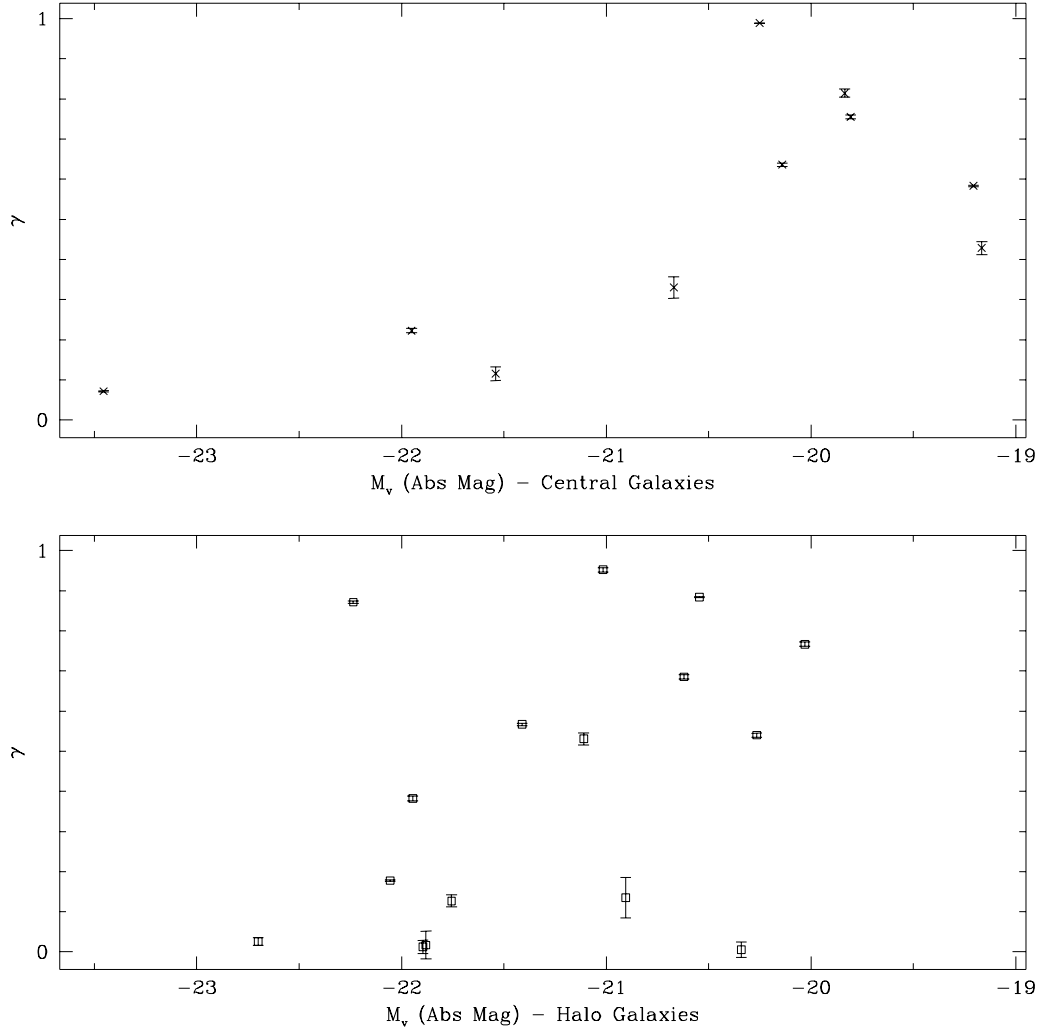


Figure 4.4: Plots of γ against M_v for the central and halo regions

convolved and deconvolved models with break radii of 0.025, 0.050 and 0.075 arcsec. By saying that the deconvolved profiles give a lower limit to the surface brightness, they have said that where the models fall below the deconvolved profile, the break radius for that model gives an upper limit for the break radius of that galaxy. This has allowed them to set upper limits of 0.05 and 0.08 (rounded from 0.075) on the break radii of some galaxies.

On other galaxies, no upper limit has been found from the models so the upper limit has been set at 0.1 arcsec, which was the upper limit of the region of the profile they were examining. As the limit of resolution for cores has been set at 0.16 arcsec, this has led to an apparent gap between the break radii of the observed cores and the maximum possible break radii of the galaxies without resolved cores.

I have used $r_{im} \approx 70$ pc (at Coma distance) ≈ 0.16 arcsec. If this is used instead of the 0.05 - 0.10 arcsec range used by Faber et al then no gap is seen between the break radii of resolved cores and the maximum break radii of unresolved cores, as is seen in the lower graph of figure 4.5 (crosses = central, boxes = halo)

4.6 Break radius vs Effective radius

Faber et al found a linear relationship between effective radius and core radius, $r_b = 0.03 r_e$, in those galaxies with resolved cores. This relationship has been plotted, with my data points, in the upper graph of figure 4.5. I do not find this relation in the galaxies with resolved cores in our sample as can be seen from this graph. Addition of more large galaxies would probably lead to a relationship being found, as it is in Faber et al, but this relationship does not appear to hold when only the smaller galaxies are considered (eg. $r_e < 10000$ pc).

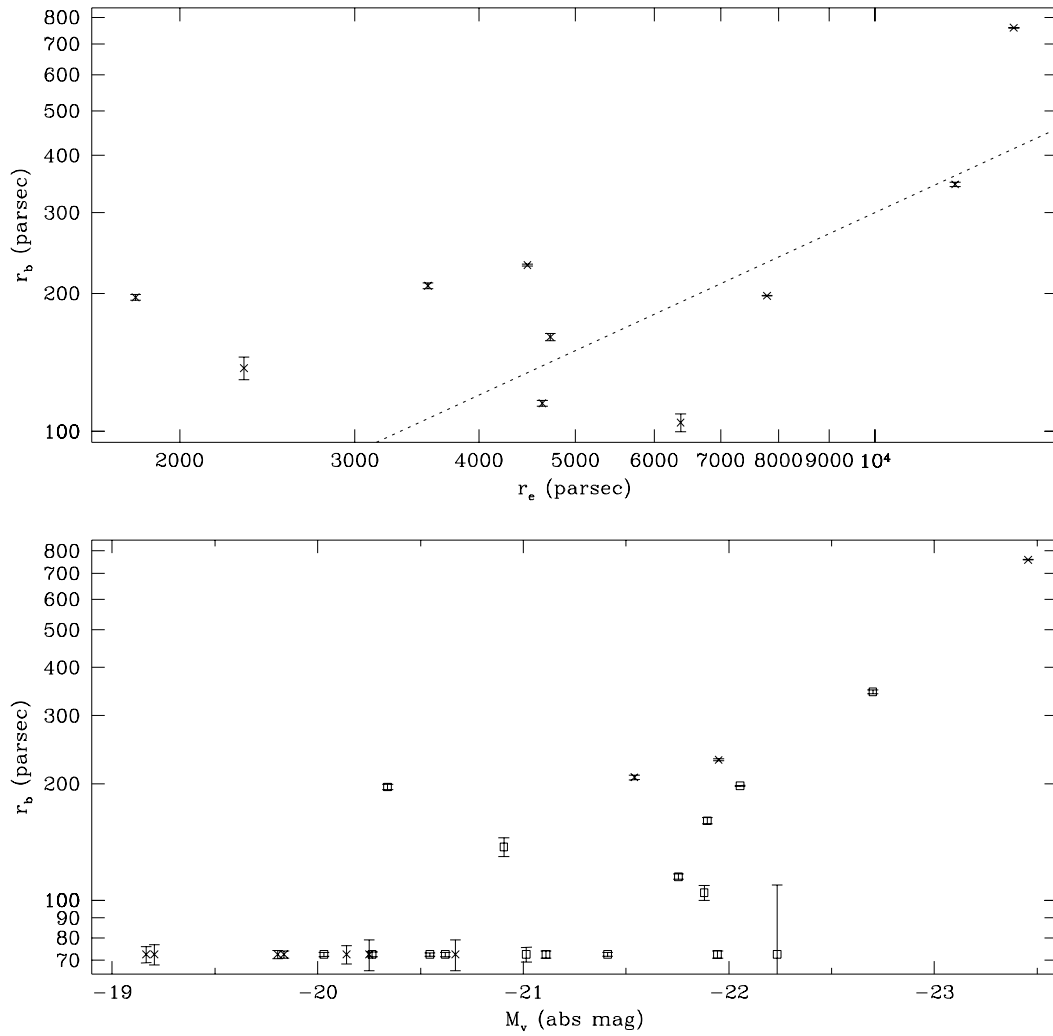


Figure 4.5: Upper - plot of r_b vs r_e for those galaxies with $\gamma < 0.3$, with the fit found by Faber et al shown by the dotted line.

Lower - Plot of r_b vs m_v with r_{lim} substituted for galaxies with $\gamma > 0.3$

4.7 Comparison with previous results

Plots of my data and Faber et al's data are in figure 4.6 My data is shown by crosses and Faber et al's by boxes.

4.7.1 M_v vs γ

The results are similar to those obtained by Faber et al (1996) below -19 magnitudes, the cut off point for our observations (see fig 4.6). I have found significantly more points with $0.3 < \gamma < 0.5$ than Faber et al and my results do not show the clear trend given by the low-luminosity tail in Faber et al's results (see fig 4.1).

4.7.2 r_b vs γ

Once again our results are very similar to Faber et al in the larger galaxies (above our limit of resolution, $\log r_b \approx 1.85$, $r_b \approx 70\text{pc}$) (see fig 4.6). Below this, all of Faber et al's results have $\gamma < 0.5$ and have either been classified as cores or as having too small a break radius to classify as resolved. The 6 galaxies in this section that were classified as having cores would not have had these cores resolved in our sample.

In the Faber et al sample, M31 has a resolved core at its true distance but this core is unresolved when it is translated to Virgo. This would appear to support the hypothesis that the core-type / power-law distinction is an effect of resolution.

4.8 Diskiness

Diskiness is defined, as described in section 3.1.1, as having a maximum value of $a_4/4$ greater than 0.02. Out of the dust-free galaxies, 9 meet this criterion. These are RB6, RB18, IC3947, IC4051 and NGC4860 from the central region and IC3618, Zw159-89, NGC4839 and NGC5004 from the

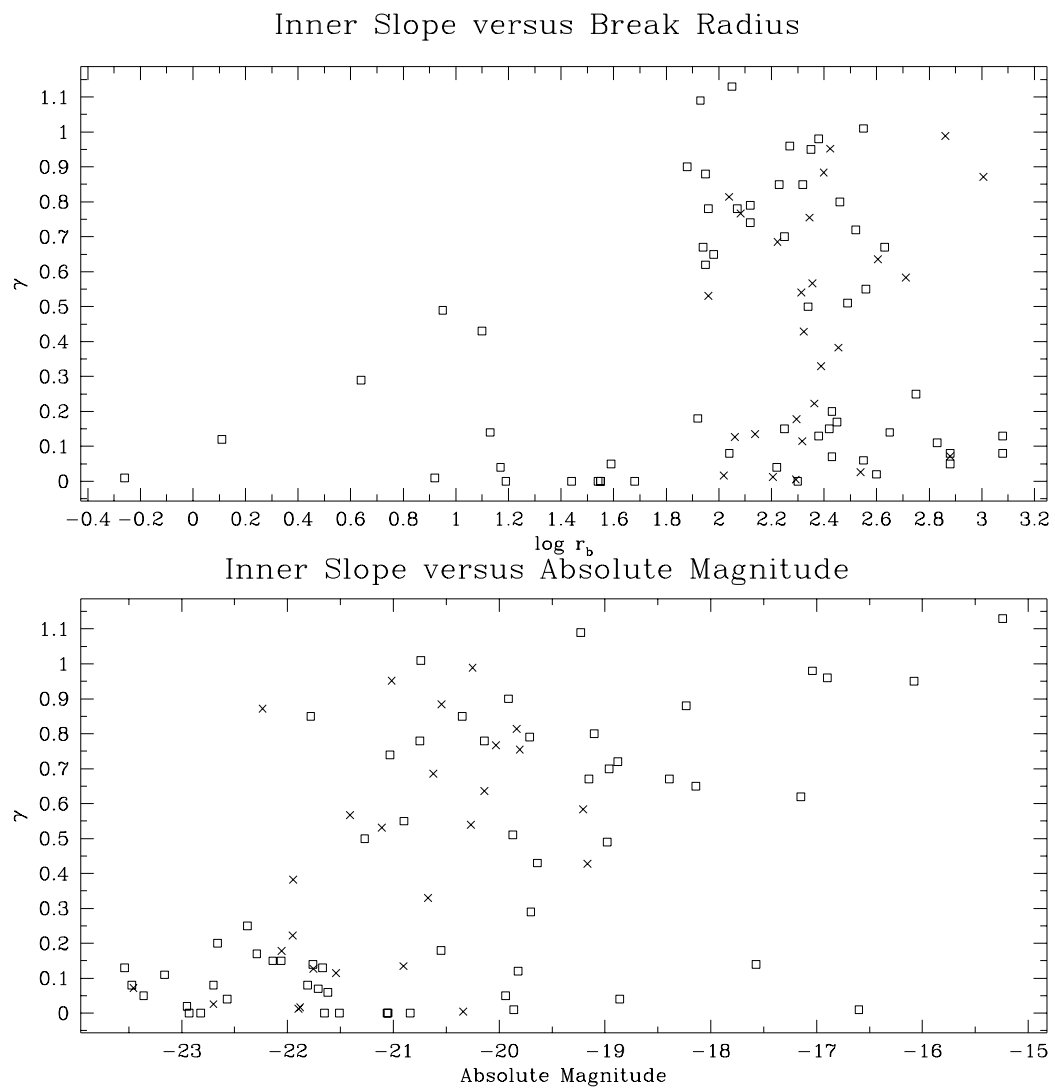


Figure 4.6: Comparison of Faber et al's data (boxes) and my data (crosses)

halo region. NGC4839 is a D-type galaxy with dust in the central region that, while it hasn't affected the fit, has led to distortion of the a^4/a term and so can be removed from this list. The $\cos 4\theta$ deviation profiles of the 8 galaxies which appear to be disk-like are given in fig 4.6. Galphot results are shown by crosses and IRAF results are shown by boxes.

The other galaxies appear to have disks on inspection of the graphs. This includes 3 galaxies (2 in the central region, 1 in the halo) which have resolved cores. All 3 of these galaxies are fairly bright (between -21.5 and -22 absolute magnitude). This appears to contradict Faber et al's assertion that galaxies with cores are boxy and galaxies with power-laws are disk-like.

4.9 Defining a Core

Throughout this report, I have used Faber et al's definition of a core as having $\gamma < 0.3$. There are galaxies such as NGC4886 (see fig 4.7) with a very well defined break but with a steep inner section. Galaxies with well-defined breaks are found over a range of values of γ - these would appear to be more than random flukes and it is possible that the low γ cores are a sub-set of whatever physical process causes these breaks to lower slopes - there is not particular reason for choosing $\gamma = 0.3$ as the cut-off rather than a higher value except for the apparent dichotomy seen at this point (see fig4.2). It is also possible that there are a number of these 'steps' in some galaxies, leading to an almost flat central core. This would require a multiple power-law fit to be accurately described.

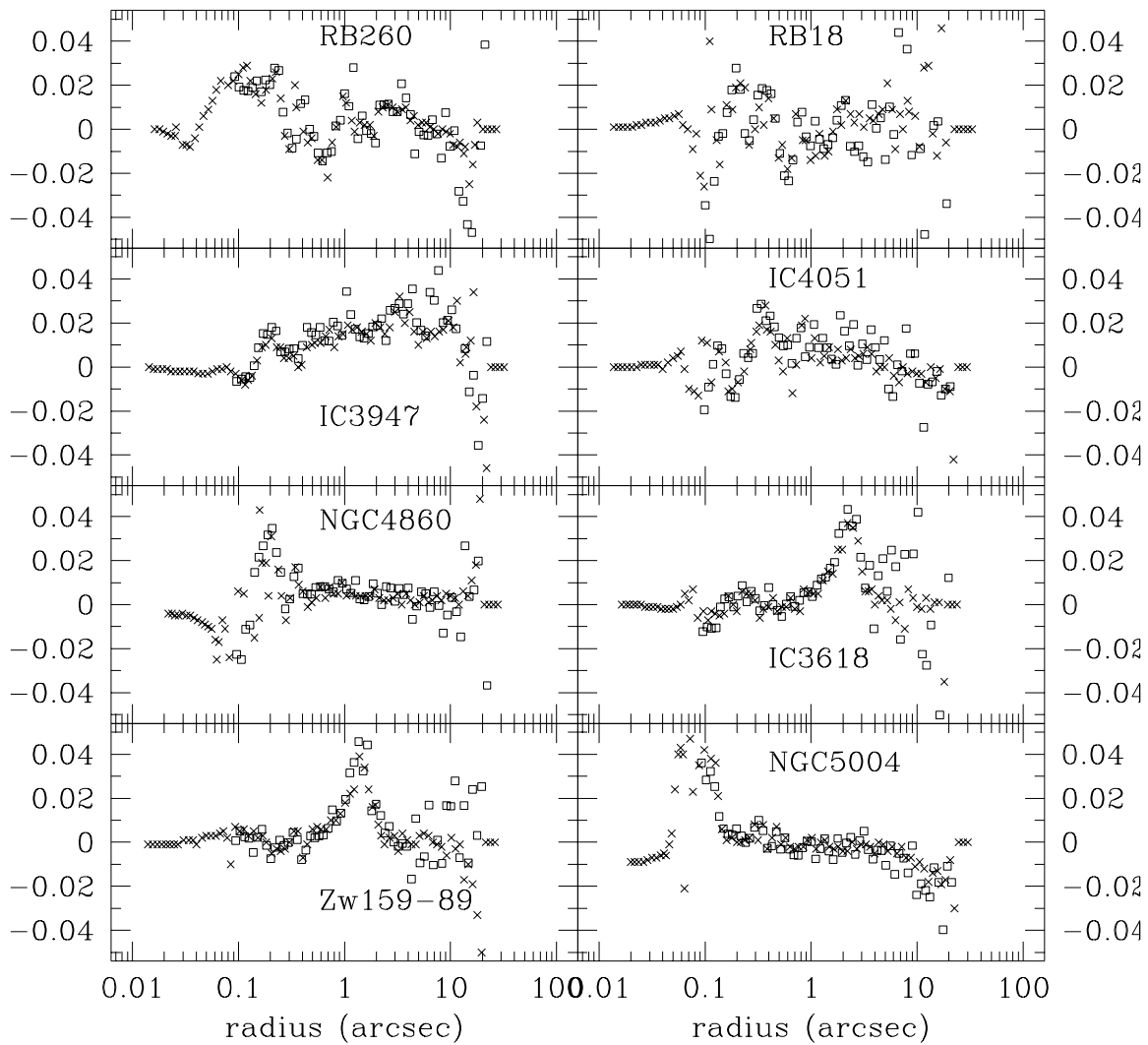
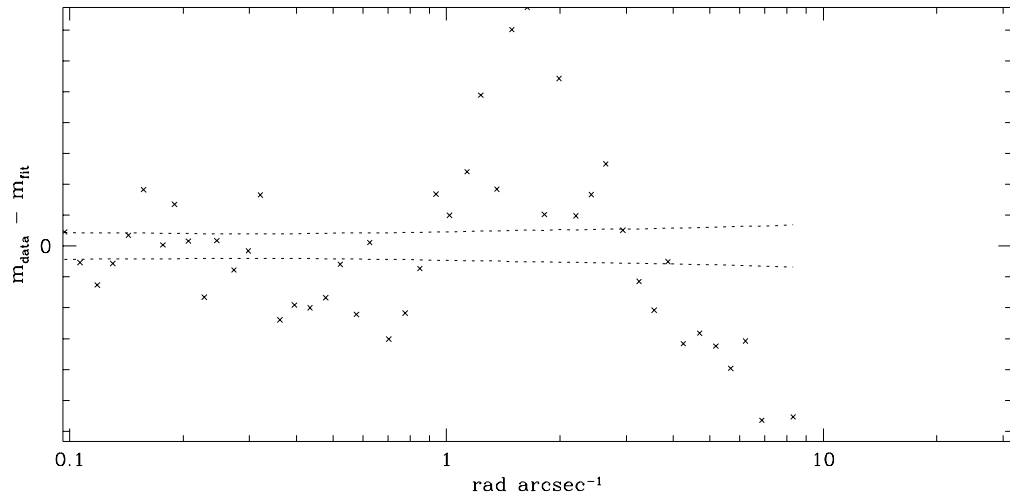
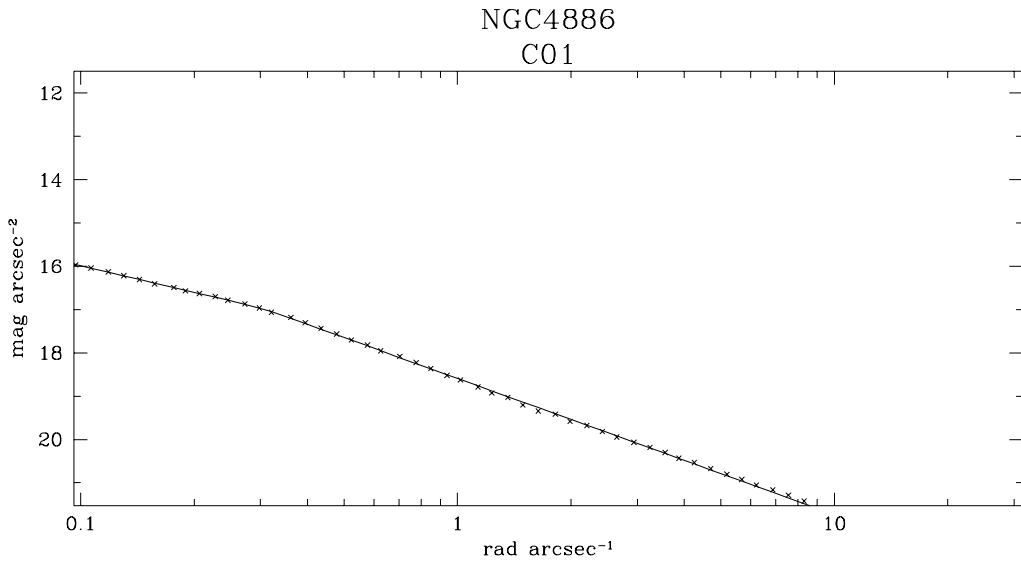


Figure 4.7: $\cos 4\theta$ terms for the 8 galaxies identified as disk. Crosses are Galphot data, boxes are IRAF data



$\alpha = 17.310965$ $\beta = 1.256647$ $\gamma = 0.812873$ $r_b = 0.307084$ $I_b = 0.158808 \times 10^{-6}$ $X = 2745.835205$
 $\delta\alpha = 2.110012$ $\delta\beta = 0.000672$ $\delta\gamma = 0.002418$ $\delta r_b = 0.001388$ $\delta I_b = 0.000763 \times 10^{-6}$ $X_v = 65.377029$
 initial values: $\alpha = 3.000000$ $\beta = 1.000000$ $\gamma = 0.500000$ $r_b = 1.000000$ $I_b = 0.100000 \times 10^{-6}$

Figure 4.8: Nuker-law fit to NGC4886

Chapter 5

Conclusions

5.1 M_v vs γ

There is no definite trend in the the data set as a whole or in the halo region sample but there is an apparent trend in the central region sample.

5.2 γ

It is shown statistically that the values of γ in both regions are probably from the same parent population. The distribution differs between the regions, with there being two distinct peaks in the distribution of gamma, as seen by Faber et al, in the halo region while there is a flat distribution in the central region.

5.3 M_v

The populations of M_v seen in the two regions are shown to be probably from different parent populations, the halo population being, on average, a magnitude brighter than the core population.

5.4 r_b vs γ

There does not appear to be a link between the value for the break-radius returned by the fitting routine and the value for γ

5.5 r_b & r_{lim} vs M_v

There is no clear evidence seen for a trend in r_b with M_v nor is the break seen by Faber et al seen when the limit of resolution is used as r_{lim} .

5.6 Diskiness

Disky galaxies are seen to be able to form cores as well as power-law profiles, this appears to indicate that it is not true that rotationally supported galaxies have power-laws and triaxial galaxies have cores.

5.7 Summary

There is a spread of break radii from the limit of resolution outwards. The gap seen by Faber et al is not apparent when the maximum possible core radius for galaxies without resolved cores is set to be the limit of resolution ($0.16''$).

The drop in the number of galaxies with $0.3 < \gamma < 0.5$ is seen only in the halo region, not in the central region.

It is seen that bright galaxies can form apparent power-laws and that disk galaxies can form cores.

No definite trend can be seen in the graphs of γ vs M_v . It is therefore not possible to use the difference in magnitudes to say that there would be a difference in the distributions of γ if the two

samples were over the same magnitude range. Therefore the difference between the two regions predicted by the gas-stellar continuum has not been proven.

Acknowledgements

I would like to thank Professor Davies, Dr de Jong and Dr Lucey for their advice and help in doing this project.

Appendix A

Errors in the ellipses

Average number of counts in an annulus = $\langle DN \rangle$

Gain = g , Average number of photons in annulus = number of electrons = $g \times \langle DN \rangle$

Number of pixels in an annulus \approx area of annulus = $2\pi r \delta r$

Read noise per pixel = σ_{rn} (in electrons)

Total read noise in annulus = $\sqrt{\sigma_{rn}^2 \times 2\pi r \delta r}$

Average read noise in annulus = $\frac{\sqrt{\sigma_{rn}^2 \times 2\pi r \delta r}}{2\pi r \delta r} = \frac{\sigma_{rn}}{\sqrt{2\pi r \delta r}}$

Total number of counts in annulus = $\langle DN \rangle \times 2\pi r \delta r$

Total number of photons in annulus = $g \times \langle DN \rangle \times 2\pi r \delta r$

Counting error in total photons, $\sigma_\gamma = \sqrt{g \times \langle DN \rangle \times 2\pi r \delta r}$

Counting error in average photons, $\sigma_{\langle \gamma \rangle} = \frac{\sqrt{g \times \langle DN \rangle \times 2\pi r \delta r}}{2\pi r \delta r} = \sqrt{\frac{g \times \langle DN \rangle}{2\pi r \delta r}}$

Total error in ellipse:

$$\begin{aligned}\sigma &= \sqrt{(\sqrt{\sigma_{\langle \gamma \rangle}})^2 + \left(\frac{\sigma_{rn}}{\sqrt{2\pi r \delta r}}\right)^2} \\ \sigma &= \sqrt{\left(\text{sqrt}\frac{g \times \langle DN \rangle}{2\pi r \delta r}\right)^2 + \left(\frac{\sigma_{rn}}{\sqrt{2\pi r \delta r}}\right)^2} \\ \sigma &= \sqrt{\frac{g \times \langle DN \rangle + \sigma_{rn}^2}{2\pi r \delta r}}\end{aligned}$$

Proportional error in average number of counts in annulus:

$$P_{\langle DN \rangle} = \frac{\sqrt{g \langle DN \rangle + \sigma_n^2}}{g \langle DN \rangle \times \sqrt{2\pi r \delta r}}$$

Appendix B

Notes on Galaxies

Those galaxies which had an offset between the centres of the galaxy in the two images of between 0.1 and 0.2 pixels are noted as such below. No note is made if the offset was less than 0.1 pixels. For the four galaxies with an offset greater than 0.2 pixels it is noted whether they had a shift less than 0.1 pixels when examined using a cross-correlation routine or whether one of the images had to be shifted in order to align it. It is also noted what evidence of dust there is in each of the galaxies and if there are any other features on the image.

- NGC4886 had a separation between the two images of between 0.1 and 0.2 pixels when they were combined. There is no evidence of dust either visibly or in the 3θ terms.
- IC4011 shows no evidence of dust either visibly or in the 3θ terms. There is a small companion galaxy or a star in the bottom-right of the frame.
- NGC4876 had a separation between the two images of between 0.1 and 0.2 pixels when they were combined. There is visible dust in the core, this also shows up in the 3θ terms.
- RB43 had a separation between the two images of between 0.1 and 0.2 pixels when they were combined. There is no evidence of dust either visibly or in the 3θ terms.

- IC3959 has visible dust in the core, this also shows in the 3θ terms.
- IC3957 shows possible visible evidence for a ring of dust around the core. This does not show up in the 3θ terms but there does appear to be a disruption in the 4θ terms. There is a companion galaxy in the bottom left of the frame.
- RB257 shows possible visible evidence for dust. This does not show up in the 3θ terms but there is a discrepancy between the 3θ terms measured by `ellipfit` and `ellipse` inside of ≈ 0.2 arcsec (4 pixels). There are a couple of stars in the bottom left of the frame. This galaxy is classified as a possible lenticular.
- RB260 shows no visible evidence of dust but there is some evidence of an asymmetry in the 3θ terms.
- NGC4869 had a separation between the two images of between 0.1 and 0.2 pixels when they were combined. There is visible dust in the core, this also shows up in the 3θ terms. There is a large star in the bottom left of the frame, there is another object to the top left and two objects to the top right.
- RB6 shows no evidence of dust either visibly or in the 3θ terms. There is a star to the top right of the frame.
- RB45 shows no evidence of dust either visibly or in the 3θ terms. There are odd ‘stretch marks’ on the `ellipfit` residual, lines projecting radially from the centre and symmetric through the centre.
- RB18 shows no visible evidence of dust but there is evidence of an asymmetry in the 3θ terms. The galaxy undergoes a visible rotation between radii of 2 and 4 arcseconds. The 4θ terms are also confused. The core appears diskly and this is supported by the $\cos 4\theta$ terms, this does not extend outwards.

- NGC4889 had the two images shifted to match them before they were combined. This is the cD galaxy and is very flat-topped. There is little visible evidence of dust but the 3θ and 4θ terms are very confused within 1 arcsecond. This is within the core radius so does not affect the conclusion that this galaxy has a soft core.
- IC4021 has visible dust in the core, this does not show particularly in the 3θ terms but there is a discrepancy between the `ellipse` and `ellipfit` terms.
- RB167 has visible dust in the core, this also shows up in the 3θ terms. The core is visibly disk-like. There is a star at the top of the frame. There are odd ‘stretch marks’ on the ellipfit residual, lines projecting radially from the centre and symmetric through the centre.
- IC4012 has visible dust in the core, this also shows in the 3θ terms.
- IC3947 shows no evidence of dust either visibly or in the 3θ terms. There are a number of small objects on the frame.
- RB234 shows no visible evidence of dust, although the 3θ terms appear confused.
- IC4051 has faintly visible dust in the core, this also shows up in the 3θ terms. There are a large number of small objects on the frame.
- NGC4860 appeared to have a separation of greater than 0.2 pixels using `center` but cross correlation using `X-register` gave a smaller shift. There is no visible evidence of dust but there is evidence of an asymmetry in the 3θ terms.
- RB241 shows no evidence of dust either visibly or in the 3θ terms.
- NGC4906 shows no evidence of dust either visibly or in the 3θ terms.
- NGC4926 had a separation between the two images of between 0.1 and 0.2 pixels when they were combined. There is no evidence of dust either visibly or in the 3θ terms.

- NGC4816 shows no visible evidence of dust but there is some evidence of an asymmetry in the 3θ terms. The `ellipfit` routine has not fitted between .5 and 1.5 pixel radius(!).
- Zw160-23 shows possible visible evidence of dust and there is evidence of an asymmetry in the 3θ terms. There is an ‘hump’ in the brightness profile at the point where the asymmetry occurs.
- IC3618 had a separation between the two images of between 0.1 and 0.2 pixels when they were combined. There is no evidence of dust either visibly or in the 3θ terms.
- Zw159-43 shows no evidence of dust either visibly or in the 3θ terms. There is a discrepancy between the `ellipse` and `ellipfit` 3θ terms near the core. There is a star in the top right of the frame.
- IC3623 shows no evidence of dust either visibly or in the 3θ terms.
- NGC4672 shows no evidence of dust either visibly or in the 3θ terms. There is a discrepancy between the `ellipse` and `ellipfit` 3θ terms within ≈ 1 arcsecond.
- NGC4692 shows no evidence of dust either visibly or in the 3θ terms.
- Zw159-83 shows visible evidence of a dust lane. From the 3θ terms, this lane extends from .5 arcseconds to 4 arcseconds. The fit continues inside .5 arcseconds. The residual is very confused at the radii of the dust lane.
- Zw159-89 shows no evidence of dust. The $\cos 4\theta$ terms show a definite disk component extending to 2 arcseconds radius.
- IC832 shows visible evidence for a dust ring around the core, this also shows faintly in the 3θ and 4θ terms and in a ‘hump’ on the brightness profile.

- NGC4789 shows a strong dust lane through the core, this also shows in the 3θ and 4θ terms and in a turn-down of the brightness profile near the centre. The `ellipfit` fit stops at about 0.3 arcseconds radius.
- NGC4807 shows no evidence of dust either visibly or in the 3θ terms.
- IC834 shows visible evidence for a dust lane around the core, this also shows in the 3θ terms.
- NGC4824 appeared to have a separation of greater than 0.2 pixels using `center` but cross correlation using `X-register` gave a smaller shift. There is no evidence of dust either visibly or in the 3θ terms.
- NGC4827 shows visible evidence for a faint dust lane in the core, this also shows in the 3θ terms.
- NGC4839 had a separation of between 0.1 and 0.2 pixels between the two images when they were combined. There is no visible evidence for dust but the 3θ and 4θ terms are very confused. It has a very flat profile, similar to that of NGC4889.
- NM8603 shows no evidence of dust either visibly or in the 3θ terms. There is a discrepancy between the `ellipse` and `ellipfit` 3θ terms near the core.
- IC4133 shows no evidence of dust either visibly or in the 3θ terms.
- NGC4952 shows visible evidence for a dust lane in the core, this also shows in the 3θ terms.
- NGC5004 had the two images shifted to match them before they were combined. There is no visible evidence for dust but there is evidence for an asymmetry in the 3θ terms.
- NGC4957 had a separation of between 0.1 and 0.2 pixels between the two images when they were combined. There is no evidence of dust either visibly or in the 3θ terms.
- Zw160-159 shows no evidence of dust either visibly or in the 3θ terms.

Appendix C

Differentials of the Nuker Law

These were calculated using the Maple symbolic processor programme. They are necessary in order to fit the nuker law to the surfacr-brightness profiles.

$$I(r) = 2^{\left(\frac{\beta-\gamma}{\alpha}\right)} I_b \left(\frac{r_b}{r}\right)^\gamma \left(1 + \left(\frac{r}{r_b}\right)^\alpha\right)^{\left(\frac{\gamma-\beta}{\alpha}\right)}$$

$$\begin{aligned} \frac{dI(r)}{d\alpha} = & 2^{\left(-\frac{\gamma-\beta}{\alpha}\right)} (\gamma - \beta) I_b \left(\frac{r_b}{r}\right)^\gamma \left(1 + \left(\frac{r}{r_b}\right)^\alpha\right)^{\left(\frac{\gamma-\beta}{\alpha}\right)} \left(\ln(2) + \ln(2) \left(\frac{r}{r_b}\right)^\alpha\right. \\ & \left. - \ln\left(1 + \left(\frac{r}{r_b}\right)^\alpha\right) - \ln\left(1 + \left(\frac{r}{r_b}\right)^\alpha\right) \left(\frac{r}{r_b}\right)^\alpha + \alpha \left(\frac{r}{r_b}\right)^\alpha \ln\left(\frac{r}{r_b}\right)\right) / \left(\alpha^2\right. \\ & \left.\left(1 + \left(\frac{r}{r_b}\right)^\alpha\right)\right) \end{aligned}$$

$$\frac{dI(r)}{d\beta} = \frac{2^{\left(-\frac{\gamma-\beta}{\alpha}\right)} I_b \left(\frac{r_b}{r}\right)^\gamma \left(1 + \left(\frac{r}{r_b}\right)^\alpha\right)^{\left(\frac{\gamma-\beta}{\alpha}\right)} \left(\ln(2) - \ln\left(1 + \left(\frac{r}{r_b}\right)^\alpha\right)\right)}{\alpha}$$

$$\frac{dI(r)}{d\gamma} = 2^{\left(-\frac{\gamma-\beta}{\alpha}\right)} I_b \left(\frac{r_b}{r}\right)^\gamma \left(1 + \left(\frac{r}{r_b}\right)^\alpha\right)^{\left(\frac{\gamma-\beta}{\alpha}\right)} \left(-\ln(2) + \ln\left(\frac{r_b}{r}\right) \alpha + \ln\left(1 + \left(\frac{r}{r_b}\right)^\alpha\right)\right) / \alpha$$

$$\frac{dI(r)}{dr_b} = \frac{2^{\left(-\frac{\gamma-\beta}{\alpha}\right)} I_b \left(\frac{r_b}{r}\right)^\gamma \left(1 + \left(\frac{r}{r_b}\right)^\alpha\right)^{\left(\frac{\gamma-\beta}{\alpha}\right)} \left(\gamma + \left(\frac{r}{r_b}\right)^\alpha \beta\right)}{r_b \left(1 + \left(\frac{r}{r_b}\right)^\alpha\right)}$$

$$\frac{dI(r)}{dI_b} 2^{(-\frac{\gamma-\beta}{\alpha})} \left(\frac{r_b}{r}\right)^\gamma \left(1 + \left(\frac{r}{r_b}\right)^\alpha\right)^{\left(\frac{\gamma-\beta}{\alpha}\right)}$$

Appendix D

Computer programmes

D.1 Numerical Recipes routines

The following Numerical Recipes routines were used in the project: `covsrt.c`, `gaussj.c`, `mrqmin.c` and `nrutil.c`.

D.2 My routines

`Project.c` reads the data in from file and calls the fitting programme `mrqmin.c`. It supplies initial values and stopping conditions for the fitting.

`Funcs.c` is called by `mrqmin.c` and returns the nuker-law and the differentials

D.2.1 `Project.c`

```
1  #include "stdio.h"
   #include "math.h"
   #include "nrutil.h"
   struct profile
5  {
       float a;
       float i;
       float di;
       char datatype;
10  struct profile *nextaddr;
   };
```

```

main()
{
15     struct profile *list, *temp;
        void display(struct profile *, int, char []);
        void fit(int, struct profile *, float *, float **, float **, float *);
        int populate(struct profile *, char[]);
        float nalamda, nchisq;
20     float *alamda, **covar, **alpha, *chisq;
        char galname[10];
        int ndata, i;

        covar=matrix(1,5,1,5);
25     alpha=matrix(1,5,1,5);

        alamda=&nalamda;
        chisq=&nchisq;

30     *alamda=-1.0;
        *chisq=0.1;

        /* Set up the list and then populate it */
35     list = (struct profile *)malloc(sizeof(struct profile));
        ndata = populate (list, galname);

        /* dump the first (blank) entry */
        temp = list;
        list = list->nextaddr;
40     free(temp);
        ndata = ndata -1;

        /* Display the contents of the list */
45     display(list, ndata,galname);

        printf("\n\t%s\n", galname);
        fit(ndata,list,alamda,covar,alpha,chisq);
}

50 void fit(int ndata, struct profile *list, float *alamda, float **covar, float \
**alpha, float *chisq)
{
    float x[ndata], y[ndata], sig[ndata], a[5];
    int ia[5];
55     int iter = 1, zcnt = 0;
    void funcs(float,float [],float *,float [],int);
    void mrqmin(float [],float [],float [],int,float [],int [],int,float *\
,float **,float *,void (*funcs)(float,float [],float *, float [],int),float *);
    int n, m;
60     struct profile *current;
    float ochi;
    FILE *out_file, *cov_file;
    char o_name[10], c_name[10], temp;
    int df = ndata;
65

    /* Open output data file */
    printf("\nEnter output filename (c?.fit.g or c?.fit.e)\n");
    scanf("%c",&temp);
    gets(o_name);
70     printf("\nEnter covariance matrix filename (c?.cov.g or c?.cov.e)\n");
    gets(c_name);
    out_file=fopen(o_name,"w");
    cov_file=fopen(c_name,"w");
    fprintf(out_file,"alpha\tbeta\tgamma\tbreak_rad\tbreak_int\tchisq\n");
75

    current = list;

    /* Setup an array with the values in */
80     for (n=1; n <= ndata; n++)
    {
        /* printf("%d ",n); */
        x[n] = current->a;
        y[n] = current->i;
85     current = current->nextaddr;

```

```

    sig[n] = current->di * y[n];
}

/*    printf("\n"); */
90
a[1] = 2.0;
a[2] = 1.0;
a[3] = 0.5;
95
a[4] = 1.0;
a[5] = 0.1;

for (n=1 ; n<=5 ; n++)
{
    printf("a[%d] = [%f].  Enter new value: ",n,a[n]);
100
    scanf("%f",&a[n]);
    /*    set which values to vary    */
    printf("vary a[%d]? (0 = no, 1 = yes): ",n);
    fprintf(out_file,"%f\t",a[n]);
    scanf("%d",&ia[n]);
105
    if (ia[n])
        ia[n] = 1;
}
fprintf(out_file,"0\n");

110
/* Note - a[5] is 1,000,000 times true value */

printf("Running Iterative Fitting Function\n");
printf("Iter.    Chisq    A[1]    A[2]    A[3]    A[4]    A[5]\n");
mrqmin(x,y,sig,ndata,a,ia,5,covar,alpha,chisq,funcs,alamda);
115
printf("%4d %12f\t%f %f %f %f %f\n",iter, *chisq, a[1], a[2], a[3], \
a[4], a[5] );
do
{
    ochi = *chisq;
120
    mrqmin(x,y,sig,ndata,a,ia,5,covar,alpha,chisq,funcs,alamda);
    iter++;
    if(ochi - *chisq > 0.01)
        zcnt = 0;
    else
125
        zcnt++;
    for (n=1 ; n<=5 ; n++)
        if (a[n]<0)
            a[n]=-a[n];
    printf("%4d %12f\t%f %f %f %f %f\n",iter, *chisq, a[1], a[2], \
130
a[3], a[4], a[5] );
}
while (((ochi - *chisq) > 0.01) || (zcnt <= 10)) || (*chisq > ochi));
*alamda=0.0;
mrqmin(x,y,sig,ndata,a,ia,5,covar,alpha,chisq,funcs,alamda);
135

for (n=1; n<=5; n++)
    df = df - ia[n];

/*    Print out values for the constants */
140
printf("\nchisq\t%f",*chisq);
printf("\nd.f.\t%i",df);
printf("\nreduced chi squared\t%f",*chisq/df);
printf("\niter\t%d",iter);
for (n=1; n<=5; n++)
145
    printf("\na[%d]\t%f\tCovar\t%f\tS.E.\t%f",n,a[n],covar[n][n],\
pow(covar[n][n],0.5));
    printf("\n");

for (n=1; n<=5; n++)
150
    fprintf(out_file,"%f\t",a[n]);
    fprintf(out_file,"%f\n",*chisq);
    for (n=1; n<=5; n++)
    {
        fprintf(out_file,"%f\t".pow(covar[n][n],0.5));
155
        for (m=1; m<=5; m++)
            fprintf(cov_file,"%f\t",covar[n][m]);
        fprintf(cov_file,"\n");
    }
}

```

```

160     fprintf(out_file,"%f\n",*chisq/df);
        fclose(out_file);
        return;
    }

165 int populate(struct profile *current, char galname[10], int *ndata)
    {
        /*      Subroutine to read the data and put it into the list      */

        FILE *in_file;
170     int n, num;
        float exptime, photzpt, photflam, err, pi;
        char galnum[4], f_name[11], h_name[8], tmp[161];
        float a,r,dr,i,s,x,y,eps,pos,s1,s2,s3,s4,c1,c2,c3,c4,f1,f2,f3,f4;
175     float meanint,rms,teta,x0,y0,slope,mag,A3,B3,A4,B4,bigA;
        char choice;

        /*      Gets a file to work upon      */
        /*      printf("\nEnter galaxy number: "); */
        /*      gets(galnum); */
180     /*      Make header file name and data file name from galaxy number */

        printf("\n Enter data file name: ");
        gets(f_name);
185     printf("\n Enter header file name: ");
        gets(h_name);
        printf("\n Enter e to fit to ellipse data, g to fit to galphot data: ");
        scanf("%c", &choice);

190     /*      Open header file      */
        in_file=fopen(h_name,"r");
        fgets(tmp,161,in_file);

        /*      Set photometric constants and read exptime      */
195     photflam = 1.8804679436201;
        photzpt = -21.100000381470;
        pi = 3.14;
        fscanf (in_file,"%f %s", &exptime, galname);
        printf("exptime = %f\n",exptime);

200     /*      Close header file      */
        fclose(in_file);

        /*      Check choice      */
205     /*      Set num (number of data) to zero */
        num = 0;

        switch(choice)
        {
170     case 'g':
            /*      Open galphot datafile */
            in_file=fopen(f_name,"r");

215     /*      Dump the first two lines      */
            for (n=0;n<2;n++)
                fgets(tmp,161,in_file);

            /*      Runs through the galphot file reading the data */
220     while (fscanf (in_file,"%f %f %f %f %f %f %f %f %f %f %f %f \
%f %f %f %f %f %f",&r,&dr,&i,&s,&x,&y,&eps,&pos,&s1,&s2,&s3,&s4,&c1,&c2,&c3,\
&c4,&f1,&f2,&f3,&f4) != EOF)
            {
225                 if ((r >= 2.0) && (i >= (exptime/100.0)))
                    {
                        /*      Set nextaddress      */
                        current->nextaddr = (struct profile *)malloc(sizeof(struct profile));
                        current=current->nextaddr;
230                     /*      Finds error in i      */
                        if (a > 20)
                            err = (pow((14.0*i+12.5)/(pi*2.0*r*(dr-r)),0.5))/(14.0*i);
                    }
            }
        }
    }

```



```

printf("\n\t%s", galname);
for (n=1; n <= ndata; n++)
310 {
    printf("\na=%f", contents->a);
    printf("\t%d", n);
    printf("\ti=%f", contents->i);
    printf("\tdi=%f", contents->di);
315     contents = contents->nextaddr;
}
return;
}

```

D.2.2 Funcs.c

```

1  #include "math.h"

void funcs(float x, float a[5], float *y, float dyda[5], int na)
{
5     float rad, k, inner, outer;

    rad = x / a[4];
    k = pow(2, (a[2] - a[3]) / a[1]);
    inner = pow(rad, -1 * a[3]);
10    outer = pow(1 + pow(rad, a[1]), (a[3] - a[2]) / a[1]);

    *y = a[5] * k * inner * outer;

    dyda[1] = *y * (a[3] - a[2]) * (log(2) + log(2) * pow(rad, a[1]) - \
15    log(1 + pow(rad, a[1])) - log(1 + pow(rad, a[1])) * pow(rad, a[1]) + a[1] * \
    pow(rad, a[1]) * log(rad)) / (pow(a[1], 2) * (1 + pow(rad, a[1])));
    dyda[2] = *y * (log(2) - log(1 + pow(rad, a[1]))) / a[1];
    dyda[3] = *y * (log(1/rad) * a[1] - log(2) + log(1 + pow(rad, a[1]))) / a[1];
20    dyda[4] = *y * (a[3] + pow(rad, a[1]) * a[2]) / (a[4] * (1 + pow(rad, a[1])));
    dyda[5] = *y / a[5];

    return;
}

```

References

- Bender, R., Burstein, D. & Faber, S. M. 1992, *Ap J*, 399, 462
- van den Bosch, F. C., Ferrarese, L., Jaffe, W., Ford, H. C. & O'Connell, R. W. 1994, *AJ*
- Byun, Y. I., Grillmair, C. J., Faber, S. M., Ajhar, E. A., Dressler, A., Kormendy, J., Lauer, T. R., Richstone, D. & Tremaine, S. *AJ*, 111, 1889
- Davies, R. L., Efstathiou, G., Fall, S. M., Illingworth, G. & Schechter, P. L. 1983, *Ap J*, 266, 41
- Faber, S. M., Tremaine, A. J., Ajhar, E. A., Byun, I. A., Dressler, A., Gebhardt, K., Grillmair, C. & Kormendy, J. 1996, Preprint
- Ferrarese, L., van den Bosch, F. C., Ford, H. C., Jaffe, W. & O'Connell, R. W. 1994, *AJ*, 108, 1598
- Gebhardt, K., Richstone, D., Ajhar, E. A., Lauer, T. R., Byun, Y. I., Kormendy, J., Dressler, A., Faber, S. M., Grillmair, C. & Tremaine, S. 1996, Preprint
- Jaffe, W., Ford, H. C., O'Connell, R. W., van den Bosch, F. C. & Ferrarese, L. 1994, *AJ*, 108, 1567
- King, I. R. 1966, *AJ*, 71, 64
- King, I. R. 1978, *ApJ*, 222, 1

- Kormendy, J., Dressler, A., Byun, Y. I., Faber, S. M., Grillmair, C., Lauer, T. R., Richstone, D.
& Tremaine, S. 1994, ESO/OHP Workshop on Dwarf Galaxies (ed. Meylan, G.)
- Lauer, T. R., Ajhar, E. A., Byun, Y. I., Dressler, A., Faber, S. M., Grillmair, C., Kormendy, J.,
Richstone, D. & Tremaine, S. 1995, *AJ*, 110, 2622
- Lucey, J. R., Guzman, R., Carter, D., & Terlevich, R. J. 1991, *M. N. R. A. S.* 253, 584
- Peletier, R., 1989, *Elliptical Galaxies - Structure and Stellar Content* (PhD Thesis)
- Press, W. H., Teukolsky, S. A., Vetterling, W. T. & Flannery, B. P. 1992, *Numerical Recipes in
C - Second Edition.*
- Wall, J. V. 1977, *Practical Statistics for Astronomers*